Using ABAQUS Cohesive Elements to Model Peeling of an Epoxy-bonded Aluminum Strip: A Benchmark Study for Inelastic Peel Arms

Ted Diehl

DuPont
DuPont Engineering Technology, Chestnut Run, Bldg 722, Wilmington, DE 19880-0722
Ted.Diehl@USA.DuPont.com

Abstract: Previous work has demonstrated the use of a penalty methodology for utilizing cohesive elements to simulate dual cantilever beam (DCB) and flexible-arm peeling problems, both involving elastic arm deformation. This approach is extended to the general case of inelastic peel arm deformations. Refinements to the original penalty selection methodology are included to account for the influence of plasticity in the peel arms. Accuracy of the method is demonstrated by comparing simulation results to experimental data of epoxy-bonded aluminum arms being peeled at different angles from a rigid substrate. This work addresses significant complexities in the analysis that arise due to the inelastic deformation of the aluminum peel arms.

Keywords: Bonding, Crack Propagation, Damage, Delamination, Failure, Fracture, Peeling, Sealing, Critical Release Energy, Critical Fracture Energy, Adhesive, Cohesive, Cohesive Zone.

1. Introduction

Previous work by Diehl (2005) has demonstrated a penalty methodology for effectively utilizing cohesive elements to simulate failure onset and failure propagation in bonded joints. The penalty framework set forth in that paper offered a plausible reconciliation of perceived differences between the classical "single-parameter G_c analytical methods" and the multiple parameter formulations required in a cohesive element or cohesive zone approach (Kinloch, 1990; Kinloch, 1994; Kinloch 2000; Blackman, 2003; Georgiou, 2003). Validity of this new penalty framework was demonstrated for two classes of problems: 1) dual cantilever beam analysis and 2) flexible-arm peeling (see Figure 1). In both cases, only elastic deformations in the arms were considered.

This current work extends the penalty-based cohesive element approach to include the important effects of *inelastic* arm deformation. Compared to the deformations occurring in a DCB specimen, it is far more likely that inelastic arm deformations will occur in flexible-arm peeling problems, and thus we concentrate on this case only. Consider common examples of peeling masking tape from a surface or peeling a thin metallized lid sealed to a drink container. After peeling, the peel arm (masking tape or metallized lid) is typically curled − evidence of inelastic arm deformation. This inelastic arm deformation can contribute significantly to the overall seal strength of the

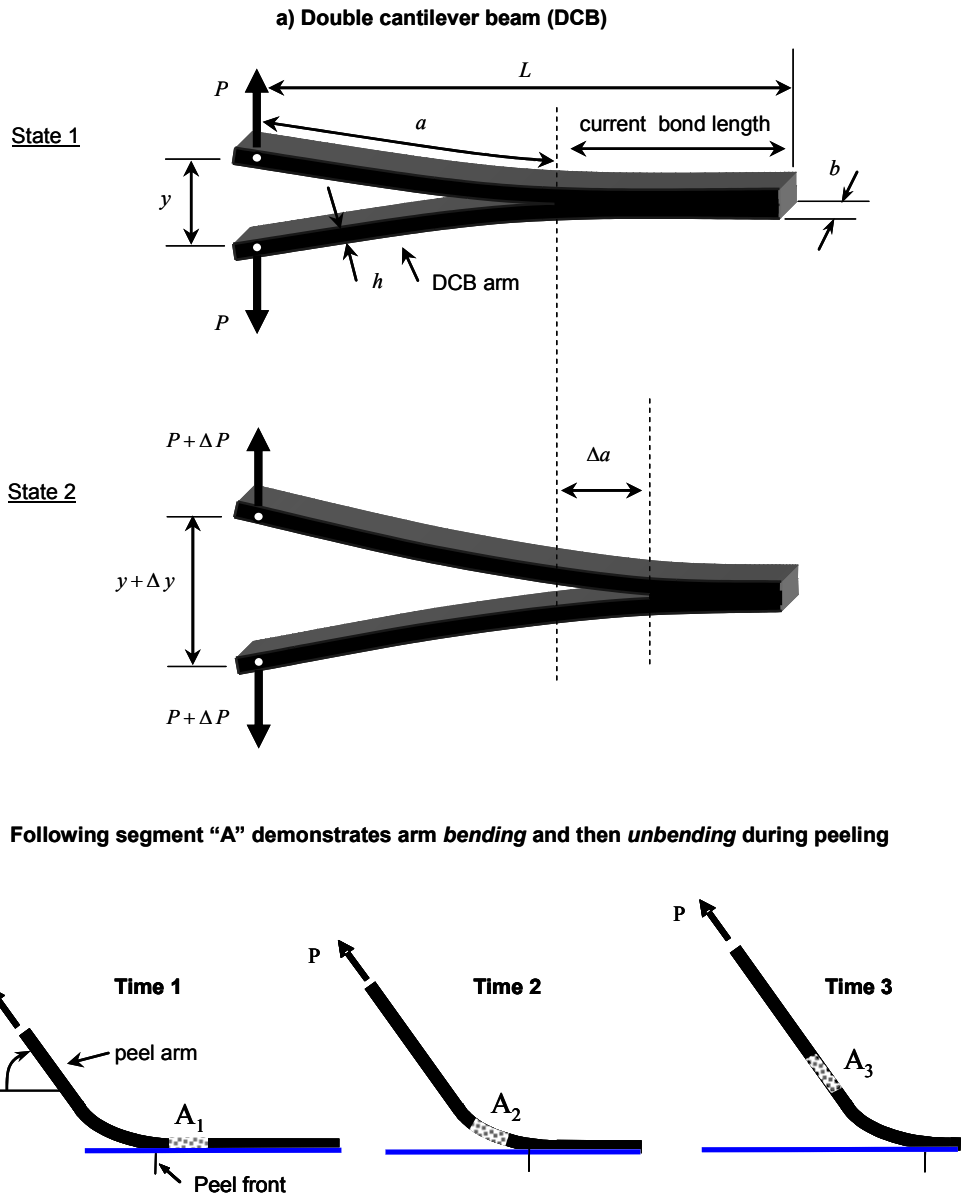

Figure 1. Idealized crack growth in a DCB specimen and the deformation history during single arm peeling.

peeling system (Georgiou, 2003; Hadavinia, 2006; Kinloch, 1990; Kinloch, 1994; Kinloch 2000) and therefore it is important to properly include its effects for a valid analysis.

2. Crack propagation via generalized Griffith energy criterion

This section provides a brief overview of the generalized Griffith energy criterion used to characterize crack propagation and peeling. This provides a foundation for understanding the underpinnings of the cohesive element approach and the importance of inelastic arm deformation.

Figure 1a depicts two beams bonded together. The bonding method could have utilized an adhesive such as "glue", ultrasonic welding, conventional welding, thermal bonding via heat sealing, or other technologies. As the tips of the beams are pulled apart, a point in the deformation history arises after which a crack extends through some portion of the bonded area. Performing an energy balance of the system as the crack propagates between states 1 and 2 in Figure 1a requires

$$\Delta U_{\text{ext}} = \Delta U_{\text{int}} + \Delta U_{\text{c}}\,, \tag{1}$$

where ΔU_{ext} represents the energy change from the externally applied load P, ΔU_{int} denotes change in stored energy in the two DCB arms, and ΔU_{c} represents the energy released as the crack extends a distance Δa. Normalizing Equation 1 by the beam depth b and crack growth Δa, and then taking the limit as $\Delta a \to 0$, we obtain

$$\frac{1}{b}\left(\frac{\mathrm{d}U_{\text{ext}}}{\mathrm{d}a}\right) = \frac{1}{b}\left(\frac{\mathrm{d}U_{\text{int}}}{\mathrm{d}a}\right) + G_c\,, \tag{2}$$

where the critical energy release rate, G_{c}, of the bond is defined as

$$G_{\text{c}} = \frac{1}{b}\left(\frac{\mathrm{d}U_{\text{c}}}{\mathrm{d}a}\right). \tag{3}$$

Re-arranging Equation 2 yields the classical form of the critical energy release rate as

$$G_{\text{c}} = \frac{1}{b}\left(\frac{\mathrm{d}U_{\text{ext}}}{\mathrm{d}a} - \frac{\mathrm{d}U_{\text{int}}}{\mathrm{d}a}\right). \tag{4}$$

The critical energy release rate is commonly referred to simply as the critical release energy or critical fracture energy. It is a material parameter that characterizes the amount of energy a bond or material releases per change in unit crack growth per unit depth. It is important to note that in using this energy-based approach to analyze the crack, we are implicitly taking a global or smeared approach to the problem, as opposed to a highly local or detailed analysis that is utilized with classical fracture mechanics methods derived around stress intensity factors, singularities, and such.

2.1 Flexible-arm peeling

Equations 1 – 4 are equally applicable to the peeling of a flexible arm as depicted in Figure 1b. If the peel arm is idealized as an infinitely rigid string (IRS), defined by infinite membrane stiffness and zero bending stiffness, and the bonding agent is assumed to have no compliance, then there will be no change in internal energy as the arm peels. The only energy change will be derived from the external load and energy released from the crack itself. Utilizing Equation 2 and simple geometry indicates that the peel load, $P_{\text{IRS}} = P$, is related to the critical release energy of the bond via

$$P_{\text{IRS}} = \frac{G_c\, b}{1-\cos(\theta)}\,. \qquad (5)$$

For most physically realizable systems, this idealization will not hold true and there will be changes in the internal energy as the peel advances (even during steady state crack growth). Sources of internal energy changes are elastic and inelastic stretching of the peel arm (left of the peel front in Figure 1b), inelastic bending of the peel arm as portions continuously transition from bonded to unbonded status, and inelastic deformations in the peel arm around the crack front caused by a complex, non-uniform stress state that includes shear.

The inclusion of these additional energy consuming mechanisms into Equation 2 leads to very complex analytical formulations that do not lend themselves to simplistic closed-form formulae. Analytical solutions based on nonlinear shear-flexible beam theory that include such inelastic terms have been published by the *Adhesion, Adhesives and Composites* research group at Imperial College, London (Kinloch, 1994; Kinloch 2000; Blackman, 2003; Georgiou, 2003). These analyses also include improved estimates of the "clamped boundary condition" at the root of the crack front, allowing for root rotation and compliance based on the elastic stiffness of a finite thickness bond and peel arm. The resulting formulation becomes quite complex with several highly nonlinear, transcendental equations needing to be solved. Fortunately the method has been coded into an easy-to-use computer program called *ICPeel* (Kinloch and Lau, 2005). [1]

An important energy contribution that ICPeel includes is the influence of inelastic *bending* and *unbending* of the peel arm. Following material segment "A" in Figure 1b, we see that an initially

---

[1] It is noted that the original publishing of the analysis method used in ICPeel had a typographical error in a term related to inelastic deformation ($f_{1ep}(k_0)$, pp. 264 of Georgiou, 2003). The error, in the third line of this term, was published as

$$-\frac{4}{(1+2N)(1+N)}k_0^{2N}\left(\frac{1-N}{1+N}\right).$$

This was corrected by Kinloch (2005) to be

$$-\frac{4}{(1+2N)(1+N)}k_0^{2N}-\left(\frac{1-N}{1+N}\right).$$

All the ICPeel calculations in this current work utilize the *corrected* version of this formulation.

straight segment in the bonded region becomes bent as at it begins to peel upward and then straightens again as the segment continues into the unbonded peel arm far away from the peel front. If the peel arm were to deform only elastically, then this set of deformations would have no net energy change because the energy to bend the segment would be returned when the segment was unbent. However, if the arm deforms inelastically, then energy will be required to bend the segment (A_2) and further energy will be required to unbend the segment (A_3). There is also the possibility that for a mild inelastic deformation case only the initial bending will be inelastic, but that the unbending may remain elastic (Kinloch, 1994; Georgiou, 2003). Relative to the energy balance defined in Equation 2, energy contributions from inelastic bending and unbending can be very large.

3. Peeling of an epoxy-bonded aluminum strip

Figure 2 depicts the peeling of an epoxy-bonded aluminum strip from a rigid substrate. Physical experimental data of peel load vs peel angle for this problem was measured by the *Adhesion, Adhesives and Composites* research group at Imperial College, London (Hadavinia and Kawashita, 2006; Kawashita, 2006). This set of data forms the basis of our benchmark.

3.1 Experimental data - benchmark

The physical descriptions of the aluminum peel arm and epoxy bond are provided in Figure 2a and the relevant characterizations of these materials are displayed in Figure 3. The experiments of Kawashita indicated that the epoxy fractured cohesively, roughly down the middle of the epoxy bond. All experiments were performed at quasi-static loading rates. The resulting peel forces displayed in Figure 2 were steady state peel forces experimentally measured for three different peel angles of 45º, 90º, and 135º.

Also displayed in Figure 2c are several analytically-based estimates of the critical release energy for the bond interface during steady-state peeling. The first set of estimates was based on the infinitely rigid string (IRS) formula (Equation 5). The second set of estimates was based on the ICPeel program. In both cases, the input data was peel angle and peel force. The ICPeel calculations also utilized material data for the aluminum and epoxy. Kawashita (2006) modeled the aluminum with a power-law plasticity model (Georgiou, 2003) using a yield stress of 85 MPa and a power-law hardening coefficient of 0.22. This power-law yield stress is slightly lower than the actual yield stress of 100.3 MPa (Figure 3a) because a best-fit compromise was required for the overall stress/strain curve when modeled with a power-law. (Only minor differences in G_c estimates were found when a yield stress of 100.3 MPa was utilized in the ICPeel power-law model). The epoxy was simply modeled as an elastic foundation (Kawashita, 2006).

For both analytical approaches, a value of G_c was calculated separately for each peel angle. The analytical approaches estimated very different values of critical release energy. The IRS method estimated values ranging from 4888 J/m^2 at 45º to 7016 J/m^2 at 135º. The ICPeel program calculated much lower values that ranged from 1333 J/m^2 at 45º to 993 J/m^2 at 135º.

Theoretically, a material characteristic such as G_c should be independent of peel angle for isotropic materials that are peeled at quasi-static rates and have the same mode of crack

a) Definition of peeling problem

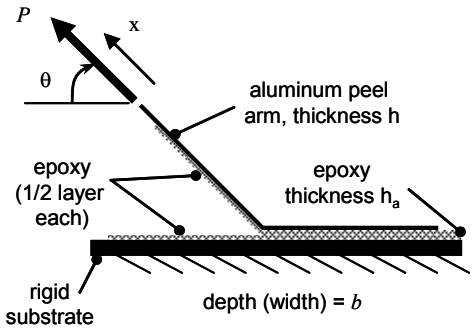

Alum. arm thickness, h (mm)	1.03
Epoxy thickness, h_a (mm)	0.307 ± 0.157
Depth, b (mm)	20

b) Measured peeling force vs peel angle

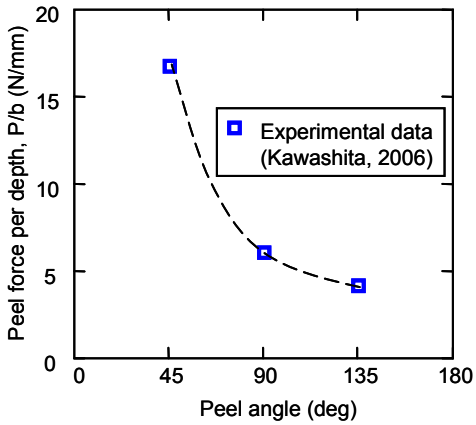

c) Estimates of Critical Release Energy computed from experimental peel force data

Peel angle, θ (deg)	**45**	**90**	**135**
Physically Measured Response			
Peel force per depth, P/b (N/mm)	16.69	6.05	4.11
Calculated Critical Release Energy, G_c			
"Infinitely rigid string" formula (J/m²)	4888	6050	7016
ICPeel program (J/m²)	1333	1147	993

Figure 2. Description of single arm peeling experiment of an aluminum substrate adhered to a rigid support via an epoxy bond.

propagation for all peel angles tested (mode I). However, both methods resulted in *angular dependent* values of G_c (variations of approximately ±15% from their 90º estimates). This angular dependence implies that these methods insufficiently represent some portion of a physical mechanism(s).

Relative to the two classes of estimates for G_c shown in Figure 2c, it is deemed that the ICPeel results are likely to be closer to the actual values since these were computed with formulae that included more physics of the problem, specifically the inclusion of inelastic deformations for bending and unbending.

a) Aluminum, ISO 5754-O, 1.0 mm thickness

True stress vs true strain, entire range

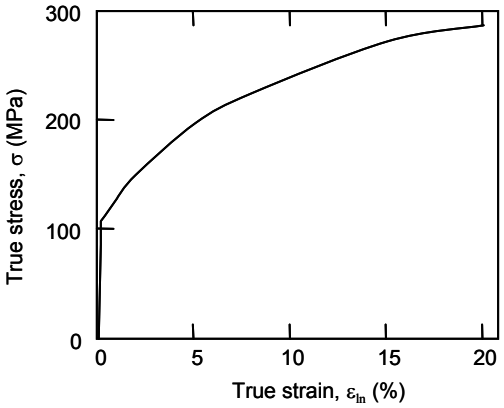

Elastic modulus (GPa)	66.0
Poisson's ratio	0.35
Density (kg/m³)	2750

*Plastic data for ABAQUS FE models

point	True Stress (MPa)	True plastic strain (%)
1	100.3	0
2	106.6	0.031
3	110.0	0.150
4	122.4	0.612
5	136.7	1.13
6	170.1	3.00
7	207.3	5.48
8	234.2	8.95
9	275.0	15.3
10	286.0	19.6

b) ESP110 Epoxy

Elastic modulus (GPa)	4.0
Poisson's ratio	0.35
Density (kg/m³)	1496

Figure 3. Material data of aluminum and epoxy utilized in finite element simulation of peeling experiment.

3.2 Finite element models

Figure 4a lists four finite element modeling approaches utilized to study the epoxy-bonded aluminum strip benchmark. The models ranged from highly detailed analyses that utilized solid element representations of the aluminum and epoxy (Figure 4c) to lower fidelity simulations that only utilized beam elements for the aluminum with no epoxy compliance (picture not shown).

a) Finite element modeling approaches analyzed

Modeling approach #	Aluminum peel arm	Epoxy compliance
1	solid elements	solid elements
2	solid elements	none
3	beam elements	solid elements
4	beam elements	none

b) Explicit transient finite element model of 135º peel at various stages during solution

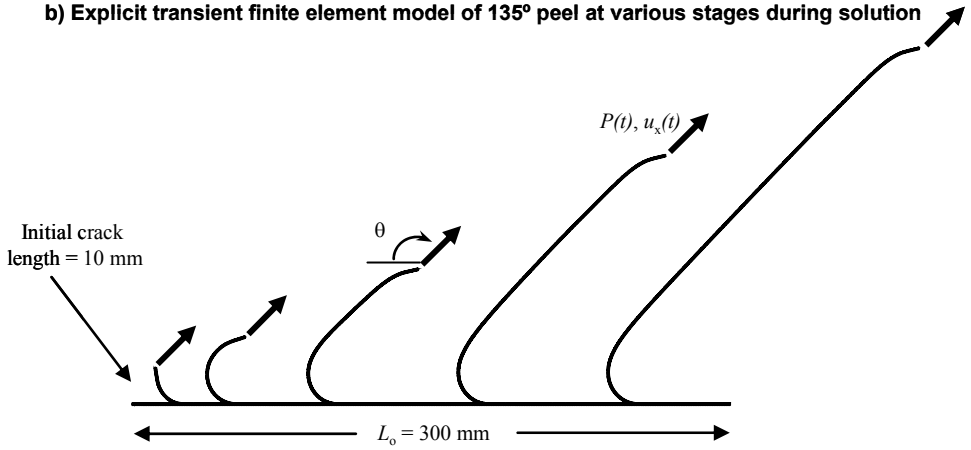

c) Highly zoomed view showing model detail near crack front (modeling approach #1)

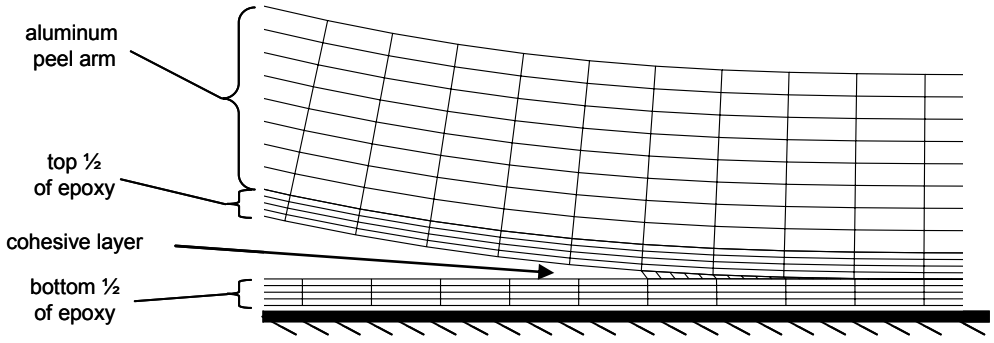

Figure 4. Various finite element modeling approaches utilized in peeling study.

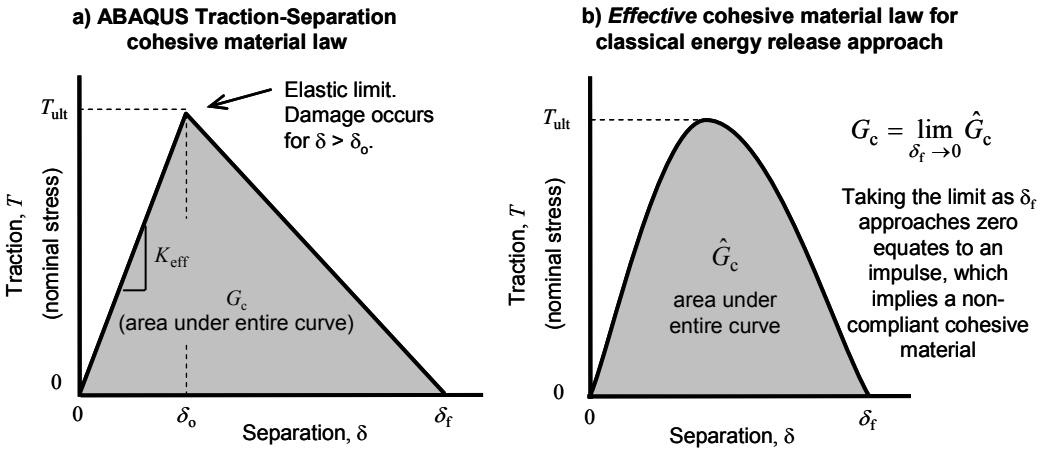

Figure 5. Traction-separation law utilized in finite element cohesive model and an interpretation of the classical Griffith energy release approach cast in a cohesive material law form.

3.2.1 Model setup

The modeling approach essentially follows that described by Diehl (2005). The cohesive failure of the epoxy bond was modeled with a zero-thickness layer of cohesive elements using a cohesive over-meshing factor of 5. The traction-separation characterization of cohesive elements is depicted in Figure 5a. The physical parameter governing the cohesive material law is G_c. Assuming an isotropic cohesive behavior, this is defined in an ABAQUS model via

```
*DAMAGE EVOLUTION, TYPE=ENERGY, MIXED MODE BEHAVIOR=BK, POWER=1.0
Gc, Gc
```

For isotropic behavior, the BK mixed mode behavior option (ABAQUS, 2005) is the easiest choice relative to input syntax effort. Since we have defined both mode I and mode II critical release energies to be the same (isotropic), the value of the related power term (a required input for BK, set to 1.0 here) will have no actual effect on the solution.

The ABAQUS cohesive element material law is described by the shape of a triangle, and thus definition of G_c alone is not sufficient. Critical release energy is related to the cohesive material's *effective* ultimate nominal stress, T_{ult}, and cohesive ductility (failure separation), δ_f, via

$$G_c = \frac{T_{ult}\,\delta_f}{2}. \tag{6}$$

Figure 5b depicts an interpretation of a traction-separation law applicable to the classical Griffith energy release approach for which the bond is assumed to be infinitely rigid until failure, at which time a finite energy is released per unit crack growth. In this interpretation, taking the limit as the cohesive ductility, δ_f, approaches zero results in an impulse function. This is deemed a reasonable interpretation of a classical Griffith energy criterion (i.e. it is defined solely by G_c and zero

compliance). Thus in the finite element cohesive material model, we view the cohesive ductility as a penalty parameter that we desire to make as small as possible until the numerical solution becomes ill-behaved. Table 1 lists ten cases of cohesive ductility used with each of the modeling methods from Figure 4a. As shown previously by Diehl (2005), the mesh-relative cohesive ductility (failure separation relative to length of cohesive elements) is the best measure of the penalty parameter intensity.

Having defined a range of δ_f, and knowing the value of G_c, we utilize Equation 6 to compute the *effective* ultimate nominal stress, T_{ult}, of the cohesive material (a dependent penalty parameter). This data is entered via

```
*DAMAGE INITIATION, CRITERION = MAXS
Tult, Tult,  Tult
```

Remember that this is not a physical material parameter, but rather a penalty term. It is not the ultimate stress of a bulk version of the bond material.

From Figure 5a, the initial material stiffness per unit area (load per unit displacement per unit area), K_{eff}, is simply

$$K_{\text{eff}} = \frac{T_{\text{ult}}}{\delta_{\text{o}}} . \tag{7}$$

Defining the *damage initiation ratio* as

$$\delta_{\text{ratio}} = \frac{\delta_{\text{o}}}{\delta_{\text{f}}} \tag{8}$$

provides a simple scalar variable ranging between 0 to 1 (exclusive) for defining when damage initiates. Combining Equations 6 - 8 shows that

$$K_{\text{eff}} = \frac{2\,G_{\text{c}}}{\delta_{\text{ratio}}\,\delta_{\text{f}}^2} . \tag{9}$$

The value of the *effective* elastic modulus of the cohesive material, E_{eff}, is related to K_{eff} via

$$E_{\text{eff}} = K_{\text{eff}}\, h_{\text{eff}} , \tag{10}$$

where h_{eff} is the initial *effective* constitutive thickness of the cohesive element. There are two options of how this thickness is defined in ABAQUS. One option is to have it defined by the actual geometric thickness derived from the nodal definitions defining the cohesive element (via `*Cohesive Section, Thickness = Geometry`). For many surface bonding applications this approach is highly problematic because the actual physical thickness of the bond (or bond material) is ill-defined or unknown. Another option is to define the geometric thickness (via nodal locations) as zero or any value that is deemed appropriate and then to manually define a

Table 1. Cohesive element modeling parameters.

a) Parameters common to all FE models studied

Cohesive over-meshing factor	5
COH2D4 elem length ΔL_{COH2D4} (mm)	0.080
Damage initiation ratio, δ_{ratio}	0.50

b) Cohesive ductility values utilized for each FE modeling approach

Case	Mesh-relative cohesive ductility $\delta_f / \Delta L_{COH2D4}$	Cohesive ductility relative to Aluminum thickness δ_f / h	Cohesive ductility relative to Epoxy thickness δ_f / h_a	Ultimate nominal stress for cohesive law T_{ult} (MPa)	Additional cohesive density scale-up factor
1	6.00	0.466	1.564	4.17	19.36
2	4.50	0.350	1.174	5.56	10.89
3	3.00	0.233	0.782	8.33	4.84
4	2.50	0.194	0.651	10.0	4.84
5	2.00	0.155	0.520	12.5	4.84
6	1.50	0.117	0.393	16.7	4.84
7	1.00	0.078	0.261	25.0	2.25
8	0.50	0.039	0.130	50.0	2.25
9	0.10	0.0078	0.0261	250.0	1.0
10	0.05	0.0039	0.0130	500.0	1.0

constitutive thickness on the `*Cohesive Section` card via the `Thickness = Specified` option. This later approach is the default method. A useful technique is to specify a *unity* constitutive thickness so that the effective modulus, which is entered on the `*Elastic` card, is actually the initial cohesive material stiffness per unit area. It also means that the strains reported in the output database for the cohesive elements are actually the separation values, δ.

From the Griffith energy release viewpoint, the cohesive element is simply representing the failure surface and thus has no thickness. Using the penalty framework for cohesive elements, it is best to directly model bond compliance with solid elements (as done in modeling approaches #1 and 3 from Figure 4a) and to utilize the cohesive elements to strictly model an idealized zero-thickness

peeling surface. Hence, we define the "nodal" cohesive element thicknesses as zero and utilize a unity value for the user specified thickness h_{eff}.

```
*COHESIVE SECTION, RESPONSE = TRACTION SEPARATION, THICKNESS = SPECIFIED,
ELSET=Glue, Material=bond
1.0,
```

Assuming a damage initiation ratio $\delta_{\text{ratio}} = 0.5$ (see Diehl, 2005 for more details) and utilizing Equations 9 and 10, we can compute the *effective* elastic modulus, E_{eff}, which is then entered via

```
*ELASTIC, TYPE = TRACTION
Eeff, Eeff, Eeff
```

Since we have chosen an Explicit modeling approach, we must supply a material density for the zero-thickness bond surface. This is not the density of the epoxy, but rather another numerical penalty parameter for the cohesive element. We simply compute an *effective* density so that the cohesive material does not, in general, unnecessarily constrain the solution time increment that the problem would otherwise require. The *effective* density, ρ_{eff}, of the cohesive material is computed via

$$\rho_{\text{eff}} = E_{\text{eff}} \cdot \left(\frac{\Delta t_{\text{stable}}}{f_{\text{t2D}} \; h_{\text{eff}}} \right)^2 \qquad (11)$$

where the stable time scale factor for 2D cohesive elements in ABAQUS is $f_{\text{t2D}} = 0.32213$ (for cohesive elements whose original nodal coordinates relate to zero element thickness) and Δt_{stable} is the initial stable time increment *without* cohesive elements in the model. The value of ρ_{eff} computed in this manner should be checked to make sure that it is not imposing too much mass in the bond area relative to the local mass of the surrounding structural materials. It is further noted that for ABAQUS version 6.5, additional density scale-up factors (Table 1) were utilized for certain cases to address some solution inefficiencies caused by an over-conservative time step estimation algorithm in ABAQUS. It is also noted the stable time scale factor which ABAQUS uses for cohesive elements ($f_{\text{t2D}} = 0.32213$) is potentially too conservative (making the solution unnecessarily inefficient). These problems have been identified to ABAQUS developers and should be addressed in a future release.

Lastly, upon complete material failure of a given cohesive element, it is desirable to direct the code to remove the failed element from the solution via

```
*SECTION CONTROLS, NAME=GLUE-CONTROLS, ELEMENT DELETION=YES
```

This option is the default behavior in ABAQUS. It is recommended that the user not override this setting to allow failed cohesive elements to remain in the solution. Doing so can create excessively slow solutions caused by inappropriate time increment estimates and can potentially create large numerical distortions caused by improper application of bulk viscosity damping on failed elements. This problem has been identified to ABAQUS developers and should be addressed in a future release. Deleting the elements upon failure caused no ill effects on any of the solutions and avoided these problems.

3.2.2 FE model results

For the analytical methods discussed in Sections 2.1 and 3.1, the value of G_c was a calculated output derived from the peel angle, peel force, geometries, and material behaviors. With cohesive elements in a finite element model, the value of G_c is a model *input* and the peel force is a model *output*. As a starting point for the FE model, we utilized the ICPeel values of G_c derived from the experimental data shown in Figure 2. Ultimately, all the FE models were analyzed for two values of G_c; namely 1.0 kJ/m^2 and 1.32 kJ/m^2. Results using these two values demonstrate the sensitivity of the different FE modeling approaches to the value of G_c.

The FE models were intended to be quasi-static analyses, but to improve solution robustness (convergence), they were solved as transient dynamic models using ABAQUS/Explicit. Figure 4b depicts several stages of a typical solution for peeling at 135º. The solution was driven by an imposed velocity boundary condition on the left end of the peel arm. For cases with solid elements in the solution (as depicted in Figure 4c), a `*Rigid Body` multipoint constraint technique was employed to apply the boundary condition on a single node, but have its effect smeared across the end cross-section of the arm. The velocity was imposed in a rotated coordinate system. To minimize transient behavior, a ramped velocity method was used which increased the velocity from zero up to a constant value during the first 10% of the solution and then was constant thereafter. Solution reaction forces from this imposed boundary condition were then utilized to obtain the applied peel force.

It is noted that Figure 4b shows the peel arm having, through-out the solution, a permanent bend at its free end. Because there was an initially *unbonded* crack length at the beginning of the solution, this small portion of material did not endure the same deformation history as the material which was initially bonded and then peeled. As the peel arm increased in length (as more was peeled free), the influence of this permanent bend was lessened and ultimately became negligible by the end of the solution. Analyzing such models with zero initial crack length (in an attempt to avoid this issue) created other problems due excessively high stresses around the crack front that generally prevented any valid solutions.

Since the explicit dynamics method utilizes a time-marching algorithm, it is desirable to artificially increase the imposed peeling rate of the problem for increased solution efficiency. The trick is to increase the imposed displacement rate up a point where the dynamic influences on the solution are still negligible, but the computational duration is as short as possible. Figure 6 demonstrates how this concept was pushed farther than typically done, while still obtaining acceptable quasi-static results. In Figure 6a, the kinetic energy from a typical peeling solution is plotted relative to the total external work. For a quasi-static solution, this level of kinetic energy relative to the external work would be considered too high because it significantly distorts the peel loads predicted by the model. However, notice how the kinetic energy rises at a constant slope after about 1/3 of the solution has developed. This implies that the kinetic energy is not causing excessive vibrations. Instead, as the aluminum is peeled free from the bond (Figure 4b), the peel arm's ever-increasing mass (traveling at constant velocity) is simply causing the kinetic energy to rise. Figure 6b demonstrates how the "kinetic force", P_{ke}, can be effectively removed from the model's raw calculation of the peel force, P_{total} (obtained directly from the FE model's reaction forces at the imposed velocity boundary location), to get an improved estimate of the quasi-static

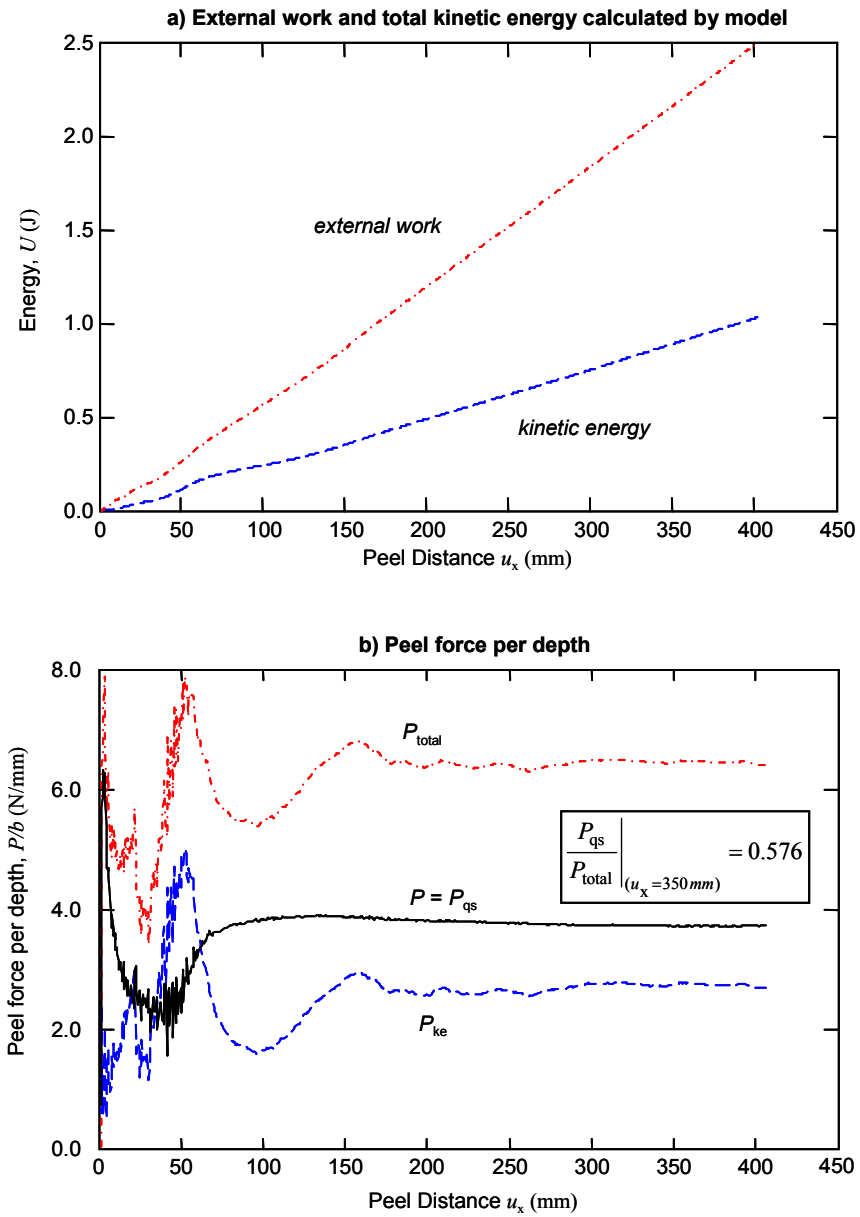

Figure 6. Improving calculation of peel load by compensating for excessive kinetic energy in Explicit model. Results shown for modeling approach #1 (solid aluminum mesh and solid epoxy mesh), Case 7 (δ_f / ΔL_{COH2D4} = 1.0), and G_c = 1.32 kJ/m^2.

peel force, P_{qs}. The kinetic force is simply computed by taking the derivative of the kinetic energy relative to the peel distance (same as crack growth assuming negligibly small peel arm stretching).

For the example depicted in Figure 6, the ratio of the resulting quasi-static peel force, P_{qs}, relative to the model's raw calculation of peel force, P_{total}, was 0.576; a significant adjustment. This technique was validated on several cases by running the models at ½ the loading rate such that the kinetic energy was ¼ its previous values. The estimates of quasi-static peel force from the two speeds were nearly identical for each case. The benefit of this kinetic force compensation technique yields computational speed-ups of 2X to 4X. For individual model computations that range between 20 minutes and 2 hours, such a savings becomes significant when over 240 different cases are run!

Figure 7a shows the influence of the mesh-relative cohesive ductility penalty on the resulting quasi-static peel force predictions for modeling approach # 1 (Figure 4a and c). Results are shown for all three peel angles. Similar to behavior reported previously by Diehl (2005), the finite element model begins to behave poorly when the mesh-relative cohesive ductility penalty is set too stiff. Due to a transitioning effect, the exact cut-off of this poor behavior is not precisely defined, but clearly occurs somewhere below $\delta_f / \Delta L_{COH2D4} = 1.0$ for the case shown here. For all the FE models in this current study, the transition range was below 1.0, but it could be different for other classes of problems (see Diehl, 2005). Figure 7b demonstrates how the "good" data (to the right of the boundary defined in Figure 7a) is further utilized to extrapolate to an "improved estimate" of peel force. This extrapolation is based on the concept that the mesh-relative cohesive ductility penalty should be 0.0 in the ideal case if numerical ill-behavior could be avoided. Since the epoxy compliance is separately modeled using solid continuum elements (in modeling approach #1 and #3), driving this cohesive stiffness to infinity is theoretically desirable (ignoring numerical problems).

It is noted that the curvature of peel force vs mesh-relative cohesive ductility shown in Figure 7b was caused by the increasing clamping stiffness of the cohesive elements around the crack front as the penalty was stiffened. This influenced the resulting inelastic deformation imposed on the peel arm. If the peel arm had behaved purely elastic, then there would be no dependency on peel force as a function of mesh-relative cohesive ductility (until the numerical ill-behavior of an excessively stiff penalty influenced the solution).

Table 2 provides a summary of all the FE model results. Accuracy of the models is judged based on normalizing the FE-predicted quasi-static peel forces relative to the actual experimental values measured by Kawashita (2006). For each modeling approach listed, two results are provided: 1) "improved estimates" based on extrapolation ($\delta_f / \Delta L_{COH2D4} = 0.0$) of peel forces via the method depicted in Figure 7b, and 2) "best direct results" using the stiffest penalty viable before numerical ill-behavior ($\delta_f / \Delta L_{COH2D4} = 1.0$). The FE model predictions are further divided into two sections, results for $G_c = 1.0$ kJ/m^2 and $G_c = 1.32$ kJ/m^2.

Ideally, the most accurate FE model should be the one with the most physics included − modeling approach #1 (all solid elements for both aluminum and epoxy). Indeed, this model demonstrated that using the "improved estimates" ($\delta_f / \Delta L_{COH2D4} = 0.0$) predicted nearly identical peel force values to the experiment for all three peel angles when $G_c = 1.32$ kJ/m^2. Most importantly, this FE model showed negligible angular dependence of G_c. Even with the "best direct results"

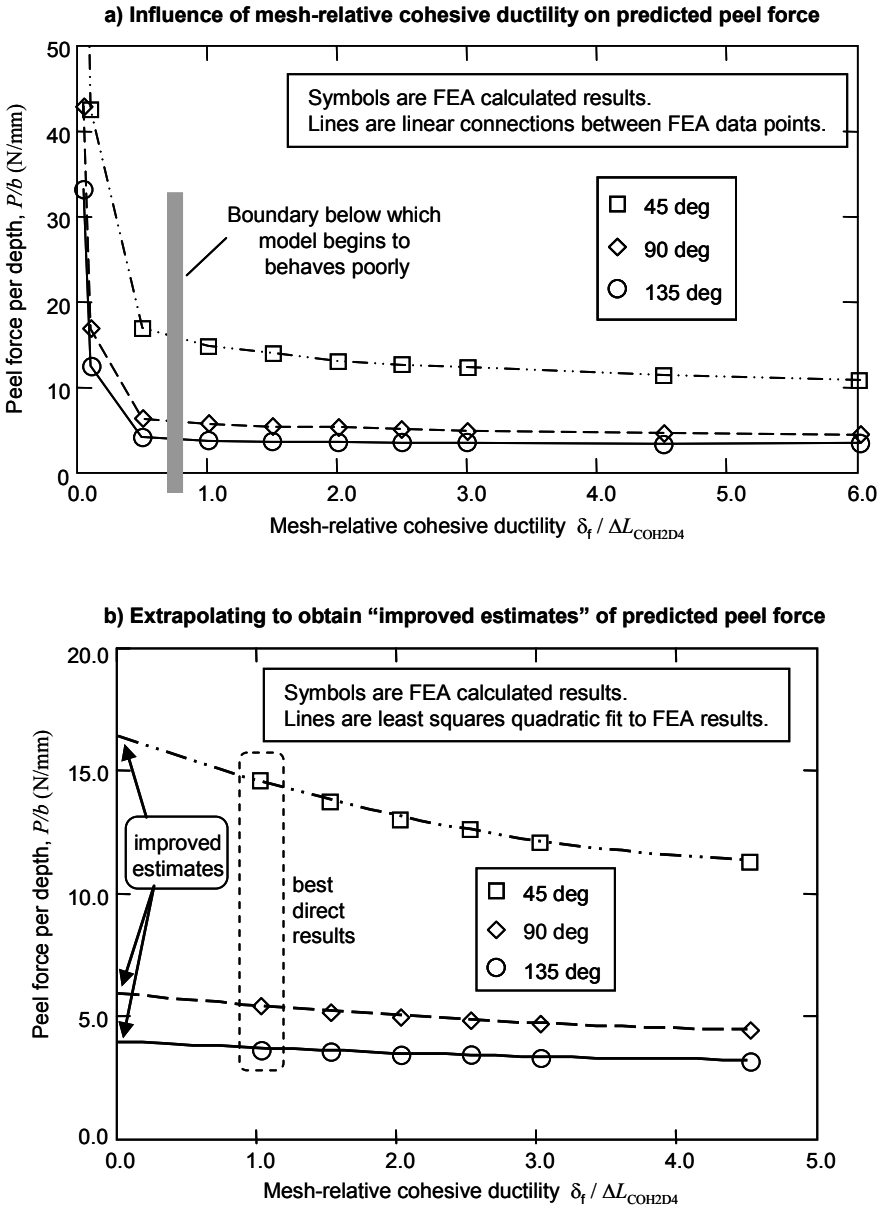

Figure 7. Influence of mesh-relative cohesive ductility on FEA predicted peel force and an extrapolation method to obtain "improved estimates." Results are for modeling approach # 1 with G_c = 1.32 kJ/m^2.

Table 2. Assessment of predictions of peel force per depth using various finite element modeling approaches.

				Peel force per depth, P/b assessment FEA calculations relative to Kawashita 2006 experiment (FEA / Experiment)		
Modeling approach #	**Aluminum peel arm**	**Epoxy compliance**	**Relative cohesive ductility** $\delta_f / \Delta L_{COH2D4}$	**45 deg peel**	**90 deg peel**	**135 deg peel**
FEA predictions using $G_c = 1.00$ kJ/m²						
1	solid elements	solid elements	0.0**	0.77	0.77	0.75
			1.0	0.68	0.70	0.71
2	solid elements	none	0.0**	0.95	1.03	1.07
			1.0	0.82	0.90	0.96
3	beam elements	solid elements	0.0**	0.95	1.000	1.05
			1.0	0.83	0.90	0.97
4	beam elements	none	0.0**	0.96	1.02	1.07
			1.0	0.84	0.91	0.99
FEA predictions using $G_c = 1.32$ kJ/m²						
1	solid elements	solid elements	0.0**	0.98	0.98	0.97
			1.0	0.88	0.90	0.91
2	solid elements	none	0.0**	1.19	1.32	1.39
			1.0	1.03	1.15	1.24
3	beam elements	solid elements	0.0**	1.16	1.28	1.33
			1.0	1.03	1.14	1.23
4	beam elements	none	0.0**	1.18	1.31	1.36
			1.0	1.04	1.16	1.26

** Mesh-relative cohesive ductility of $\delta_f / \Delta L_{COH2D4} = 0.0$ represents extrapolated values.

(δ_f / ΔL_{COH2D4} = 1.0), this model showed very little angular dependence of G_c. This also held true for this model when a value of G_c = 1.0 kJ/m^2 was utilized, albeit the predicted peel forces were about 25% lower than the experiment (as expected since G_c was lower). Modeling approach #2 indicates that removing the epoxy compliance caused the model to exhibit noticeable angular dependence as well as a slightly higher overall peel force. Because the epoxy compliance was removed, inaccurate clamping stiffness is imposed to the aluminum peeling arm, causing incorrect amounts of inelastic deformation to occur.

It is noted that others (Georgiou, 2003) have rationalized the initial stiffness of a cohesive element material law, K_{eff} (Equation 9), to represent components such as the epoxy stiffness. This leads to a model based on a linear elastic foundation approach which does not sufficiently capture the complex stiffness interactions that occur at the peel front. The FE models here demonstrate that the most accurate results are obtained when the individual materials are analyzed as continuums (solid elements) and that the cohesive element is strictly used to model the actual fracture interface.

When the aluminum peel arm was modeled with beam elements (modeling approach # 3 and 4), a value of G_c = 1.0 kJ/m^2 best fit the experimental peel force data. However, in all of these cases the model exhibited noticeable angular dependence (although not as much as the ICPeel model, Figure 2c). It is also noted that the epoxy compliance had much less influence on the results for the beam models as compared to the solid models (modeling approach # 1 and 2). This is likely because the beam models are not able to sufficiently capture the complex inelastic stress state that is occurring around the peel front in the peel arm.

3.2.3 Benchmark summary

Three different types of "models" were evaluated: the idealistic IRS model, the ICPeel model, and the various FE models. For this study, only the continuum-based FE model using cohesive elements defined in a penalty framework was able to accurately model an inelastic peeling problem with negligible angular dependence of critical release energy G_c. Direct modeling of all the physical components in the system and the proper penalty approach for the cohesive elements were the primary reason for this success.

Of the two analytical models studied, the calculated critical release energy values from the ICPeel model were generally similar to those of the FE models (as compared to the predictions from the IRS model). However the ICPeel model exhibited angular dependence of G_c. It is believed that the primary deficiency in this model is related to its beam-based formulation's inability to fully analyze the complex continuum stress state around the peel front, including the 2-D stiffness interactions between the epoxy and aluminum. Despite this limitation, the ICPeel model has significant value in that it computes extremely fast (1 – 2 seconds) and it predicts G_c values that are similar (on average) to the much more computationally intense FE models.

4. Practical modeling considerations

The methodology utilized for the FE models was quite detailed and computationally intensive in both computation time, number of models run, and extrapolation methods to obtain "improved

estimates." In many practical cases, such rigor may not be required. As the analyst repeatedly works with a similar class of problems, the need for constantly running mesh-relative cohesive ductility studies will lessen. They may be able to simply run various analyses using a single setting for the penalty ("best direct results").

Another issue to further consider is the influence and meaning of the *effective* ultimate nominal stress, T_{ult}, of the cohesive material (Figure 5a). As stated previously, this is just a dependent penalty parameter that is directly related to the physical value of G_c and the penalty value of cohesive ductility, δ_f. As the cohesive ductility penalty is stiffened, the value of T_{ult} will increase. Since this stress will be the stress acting normal to the cohesive element at the time that damage initiates and the crack begins to propagate, its value can have an influence on the solution. In particular, if its value is set higher than the maximum allowable stress that the adjacent material connected to the cohesive element can endure, then a solution will not be possible and the simulation will terminate. In this case, the cohesive ductility penalty will be clearly too stiff for the physics of the problem defined. This result might be viewed as physically reasonable. Adhering a weak material (relatively low ultimate strength) with a high strength bond (G_c is high) is likely to cause bulk material failure in the weak material, not a failure in the bond interface. This is consistent with the general behavior predicted by a cohesive model based on the penalty methodology. This also points out that the value of stress normal to the cohesive element near the crack front is ill-defined in that it is driven by a penalty parameter. This is consistent with the view that in using an energy-based approach to analyze the crack, we are implicitly taking a global or smeared approach to the problem, as opposed to a highly local or detailed analysis that is utilized with classical fracture mechanics methods derived around stress intensity factors, singularities, and such. The user needs to be mindful of these inter-relationships when analyzing such problems.

5. Conclusions

This study has presented accurate simulations of the peeling of an epoxy-bonded aluminum strip from a rigid substrate. All the models were compared to experimental results. Relative to the various analytical and FE models evaluated, it has been shown that only the continuum-based FE model, using cohesive elements defined in a penalty framework, was able to accurately model the inelastic peeling problem with negligible angular dependence of critical release energy G_c. The ability of this particular FE model to fully analyze the complex stress state in the peel front, including the 2-D stiffness interactions between the epoxy and aluminum, was the primary reason for its accuracy. This study further demonstrated how to rationally determine the cohesive ductility penalty required to convert the cohesive element approach into a single-parameter model dependent on the physically meaningful value of G_c. The work also confirmed the usefulness of the highly efficient ICPeel model and provided a potential explanation of why the ICPeel method exhibits mild angular dependence of G_c.

6. References

1. ABAQUS, *ABAQUS Version 6.5 Documentation*, ABAQUS, Inc., 2005.

2. BSI, "Determination of Mode I Adhesive Fracture Energy, G_{IC}, of Structural Adhesives using the Double Cantilever Beam (DCB) and Tapered Double Cantilever Beam (TDCB) Specimens", British Standard BS 7991:2001, October 23, 2001.
3. Blackman, B. R. K., Hadavinia, H., Kinloch, A. J., Williams, J. G., "The Use of a Cohesive Zone Model to Study the Fracture of Fibre Composites and Adhesively-bonded Joints," *International Journal of Fracture,* 119, pp 25-46, 2003.
4. Blackman, B. R. K., Kinloch, A. J., *Protocol for the Determination of Mode I Adhesive Fracture Energy, G_{IC}, of Structural Adhesives using the Double Cantilever Beam (DCB) and Tapered Double Cantilever Beam (TDCB) Specimens*, Version 00-08, European Structural Integrity Society, June 22, 2000.
5. Broek, D. *Elementary Engineering Fracture Mechanics,* Martinus Nijhoff, 1986.
6. Diehl, T., "Modeling Surface-Bonded Structures with ABAQUS Cohesive Elements: Beam-Type Solutions," ABAQUS User's Conference, Stockholm, Sweden, May, 2005.
7. Diehl, T., Carroll, D., Nagaraj, B., "Applications of DSP to Explicit Dynamic FEA Simulations of Elastically-Dominated Impact Problems," Shock and Vibration, Vol 7, pp. 167-177, 2000.
8. Georgiou, I., Hadavinia, H. H., et. .al., "Cohesive Zone Models and the Plastically Deforming Peel Test, " *Journal of Adhesion*, 79, pp. 239-265, 2003.
9. Hadavinia, H., Kawashita, L., Kinloch, A. J., et. al., "A Numerical Analysis of the Elastic-Plastic Peel Test, " *29th Adhesion Society Meeting*, Jacksonville, Florida, Feb, 2006.
10. Kawashita, L., *PhD Thesis of Luiz Kawashita*, Imperial College, London, to be published 2006.
11. Kinloch, A. J., *Adhesion and Adhesives*, Chapman and Hall, 1990.
12. Kinloch, A. J., Personal communications, 2005.
13. Kinloch, A. J., Hadavinia, H., et. al., "The Peel Behavior of Adhesive Joints," *Proc. of the Annual Meeting of the Adhesive Society*, 2000, 23rd edition.
14. Kinloch, A. J., Lau, C. C., and Williams, J. G., "The Peeling of Flexible Laminates," *International Journal of Fracture,* 66, pp 45-70, 1994.
15. Kinloch, A. J., Lau, C. C., and Williams, J. G., *ICPeel, Gc Analysis for Peel Testing of Adhesives*, Excel computer program, Imperial College, London, revised release July 24, 2005, www.imperial.ac.uk/me

7. Acknowledgment

The author is grateful to Professor A. J. Kinloch, Imperial College, London, for his initial suggestion of this benchmark problem (aka *The Kinloch Challenge*) and his many interactions throughout this project. The continued communications with ABAQUS developers Harry Harkness, Kingshuk Bose, and David Fox are acknowledged. The support of DuPont colleagues Mark A. Lamontia, Clifford Deakyne, Delisia Dickerson, Leo Carbajal, Jay Sloan, James Henderson, David Roberts, Patrick Young, and James Addison is also recognized.